JCI The Journal of Clinical Investigation

DEGS1-associated aberrant sphingolipid metabolism impairs nervous system function in humans

Gergely Karsai, … , Thorsten Hornemann, Ingo Kurth

J Clin Invest. 2019;129(3):1229-1239. https://doi.org/10.1172/JCI124159.

Clinical Research and Public Health | Genetics | Metabolism

Graphical abstract

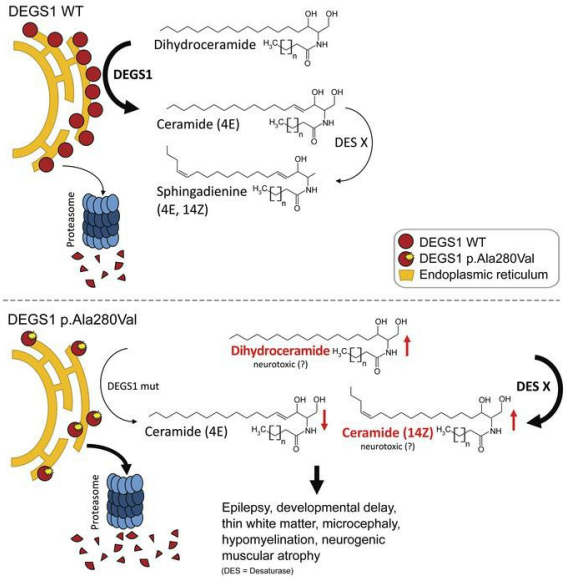

Find the latest version:

https://jci.me/124159/pdf

DEGS1-associated aberrant sphingolipid metabolism impairs nervous system function in humans

Gergely Karsai,[1,2] Florian Kraft,[3] Natja Haag,[3] G. Christoph Korenke,[4] Benjamin Hänisch,[3] Alaa Othman,[1,2] Saranya Suriyanarayanan,[1,2] Regula Steiner,[1,2] Cordula Knopp,[3] Michael Mull,[5] Markus Bergmann,[6] J. Michael Schröder,[7] Joachim Weis,[7] Miriam Elbracht,[3] Matthias Begemann,[3] Thorsten Hornemann,[1,2] and Ingo Kurth[3]

[1]Center for Integrative Human Physiology, University of Zürich, Zürich, Switzerland. [2]Institute for Clinical Chemistry, University Hospital, Zürich, Switzerland. [3]Institute of Human Genetics, Medical Faculty, RWTH Aachen University, Aachen, Germany. [4]Clinic for Neuropediatrics and Congenital Metabolic Diseases, University Clinic for Paediatrics and Adolescent Medicine, Oldenburg, Germany. [5]Department of Diagnostic and Interventional Neuroradiology, Medical Faculty, RWTH Aachen University, Aachen, Germany. [6]Institute for Neuropathology, Hospital Bremen-Mitte, Bremen, Germany. [7]Institute of Neuropathology, Medical Faculty, RWTH Aachen University, Aachen, Germany.

BACKGROUND. Sphingolipids are important components of cellular membranes and functionally associated with fundamental processes such as cell differentiation, neuronal signaling, and myelin sheath formation. Defects in the synthesis or degradation of sphingolipids leads to various neurological pathologies; however, the entire spectrum of sphingolipid metabolism disorders remains elusive.

METHODS. A combined approach of genomics and lipidomics was applied to identify and characterize a human sphingolipid metabolism disorder.

RESULTS. By whole-exome sequencing in a patient with a multisystem neurological disorder of both the central and peripheral nervous systems, we identified a homozygous p.Ala280Val variant in DEGS1, which catalyzes the last step in the ceramide synthesis pathway. The blood sphingolipid profile in the patient showed a significant increase in dihydro sphingolipid species that was further recapitulated in patient-derived fibroblasts, in CRISPR/Cas9–derived *DEGS1*-knockout cells, and by pharmacological inhibition of DEGS1. The enzymatic activity in patient fibroblasts was reduced by 80% compared with wild-type cells, which was in line with a reduced expression of mutant DEGS1 protein. Moreover, an atypical and potentially neurotoxic sphingosine isomer was identified in patient plasma and in cells expressing mutant DEGS1.

CONCLUSION. We report DEGS1 dysfunction as the cause of a sphingolipid disorder with hypomyelination and degeneration of both the central and peripheral nervous systems.

TRIAL REGISTRATION. Not applicable.

FUNDING. Seventh Framework Program of the European Commission, Swiss National Foundation, Rare Disease Initiative Zurich.

Introduction

Sphingolipids (SLs) are fundamental components of eukaryotic cell membranes where they play crucial roles in membrane architecture and signaling (1). They are major components of the myelin sheath and of fundamental importance for neural function (2). Whereas oligodendrocytes support and insulate neurons of the central nervous system, equivalent function is provided by Schwann cells in the peripheral nervous system. Besides a role in myelin sheath formation and maintenance, signaling SLs such as sphingosine-1-phosphate (S1P) and ceramide-1-phosphate are bioactive lipid hormones that regulate a variety of physiological functions. Ceramides are central components of SL metabolism, as they form the building blocks for complex SLs like sphingomyelin (SM) and glycosylceramides. They also represent the crossroad for the degradation and salvage pathways (3). Ceramide biosynthesis starts at the endoplasmic reticulum (ER) with the conjugation of L-serine and palmitoyl-CoA, the rate-limiting step catalyzed by serine palmitoyltransferase (SPT). The immediate product 3-keto-sphinganine is reduced to sphinganine (SA), which is then *N*-acylated to dihydroceramide (dhCer) by 1 of 6 ceramide synthase isoforms (CerS1–6) (4). In the final step, dhCer is converted to ceramide by the insertion of a Δ4,5 *trans* (Δ4E) double bond into the SA backbone. This final conversion is catalyzed by the Δ4-dihydroceramide desaturase DEGS1 (5). On the catabolic side, ceramides are deacylated by ceramidases to form sphingosine (SO), which can be either recycled back to ceramides (sal-

Authorship note: GK, FK, and NH contributed equally to this work. TH and IK contributed equally to this work.
Conflict of interest: The authors have declared that no conflict of interest exists.
License: Copyright 2019, American Society for Clinical Investigation.
Submitted: August 10, 2018; **Accepted:** December 21, 2018.
Reference information: *J Clin Invest*. 2019;129(3):1229–1239.
https://doi.org/10.1172/JCI124159.

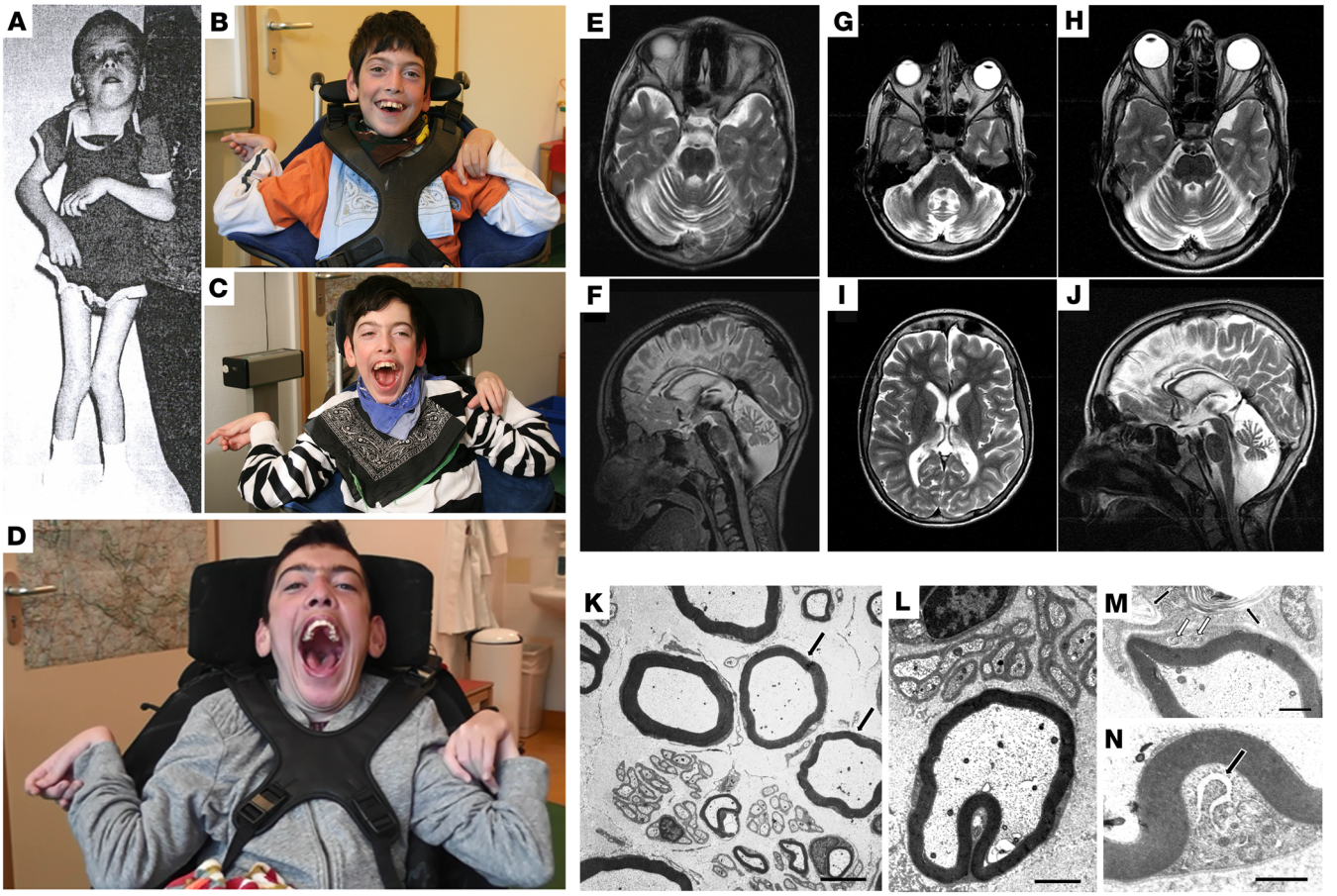

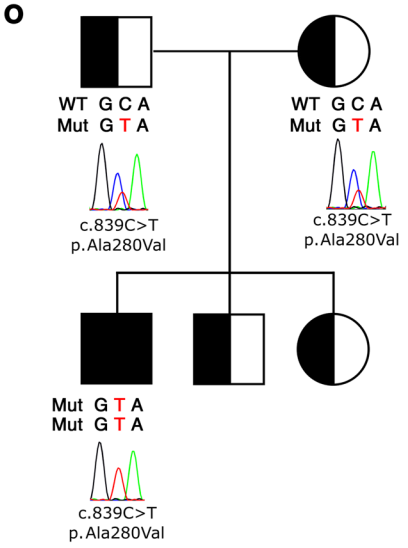

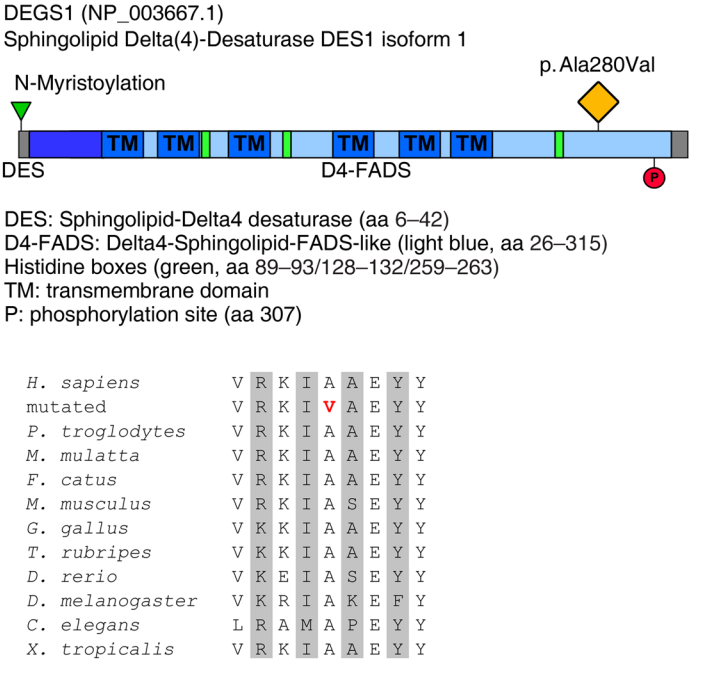

Q

H. sapiens	V	R	K	I	A	A	E	Y	Y
mutated	V	R	K	I	**V**	A	E	Y	Y
P. troglodytes	V	R	K	I	A	A	E	Y	Y
M. mulatta	V	R	K	I	A	A	E	Y	Y
F. catus	V	R	K	I	A	A	E	Y	Y
M. musculus	V	R	K	I	A	S	E	Y	Y
G. gallus	V	K	K	I	A	A	E	Y	Y
T. rubripes	V	K	K	I	A	A	E	Y	Y
D. rerio	V	K	E	I	A	S	E	Y	Y
D. melanogaster	V	K	R	I	A	K	E	F	Y
C. elegans	L	R	A	M	A	P	E	Y	Y
X. tropicalis	V	R	K	I	A	A	E	Y	Y

Figure 1. Clinical phenotype and genetics of the DEGS1 disorder. Clinical phenotype with progression of spasticity, notably in the arms and hands. Patient at the age of 6 years (**A**), 13 years (**B**), 15 years (**C**), and at last followup at 22 years (**D**). T2-weighted MRI of the brain, axial (**E**, and **G**–**I**) and sagittal (**F** and **J**), at 11 years of age (**E** and **F**) and 16 years (**G**–**J**). Severe and slowly progressive cerebellar atrophy with fiber degeneration of the middle cerebellar peduncles. The patient shows mild cortical atrophy and thin white matter, especially in the posterior brain regions. In summary, MRI findings are in line with a progressive global neurodegenerative process. (**K**–**N**) Electron micrographs of the sural nerve biopsy performed at the age of 2 years reveals nerve fibers with disproportionately thin myelin sheaths (**K**, arrows). Scale bar: 3 μm. (**L**) Occasional, moderate myelin folding. Scale bar: 1.8 μm. (**M**) Small autophagic vacuoles in the cytoplasm of the Schwann cell of a myelinated nerve fiber (white arrows). Black arrows indicate large autophagic vacuoles containing membranous debris in an adjacent cell, which is covered by a basal lamina and may therefore be either a Schwann cell or a macrophage that has invaded a Schwann cell basal lamina sheath. Scale bar: 0.75 μm. (**N**) Widening of the endoplasmic reticulum (arrow) of a Schwann cell. Scale bar: 0.5 μm. (**O**) The pedigree of the family shows the segregation of the *DEGS1* variant [NM_003676.3:c.839C>T, p.Ala280Val, Chr1(hg19):g.224380047C>T]. Sanger traces of the affected codon are shown in the index patient and his parents. (**P**) Domain architecture of the human DEGS1 protein. Position of the mutation is indicated in orange. (**Q**) Species alignment of the amino acid residues in proximity of the DEGS1 mutation. Mutation highlighted in red. FADS, fatty acid desaturase domain.

vage pathway) or phosphorylated by SO kinases (SK1/SK2) to form sphingosine-1-phosphate (S1P). S1P is a potent lipid hormone that binds to specific S1P receptors (SP1R1–6), which control a multitude of cellular responses (6). S1P can either be converted back to SO through action of S1P phosphatases (S1PPase), or terminally degraded by the S1P lyase (*SGPL1*) to hexadecenal and ethanolamine phosphate (7). For complex SL formation, ceramides are transported from the ER to the Golgi and are converted into phosphosphingolipids (e.g., SM) or glycosphingolipids (GalCer, GluCer). Subsequently, they are metabolized to highly complex glycosphingolipids such as gangliosides (8).

The degradation of complex SLs requires dedicated catabolic enzymes, such as glycohydrolases and sphingomyelinases that reside in the plasma membrane, ER, Golgi apparatus, and lysosomes (9, 10). Defects in these catabolic enzymes cause sphingolipidoses such as Fabry, Gaucher, Farbers, Niemann-Pick, and Tay-Sachs (11). Defects in the synthesis pathway are also associated with disease. Mutations in SPT (*SPTLC1* and *SPTLC2*) lead to the formation of aberrant and neurotoxic 1-deoxysphingolipids, which result in hereditary sensory and autonomic neuropathy type I (OMIM #162400, #613640) (12). Genetic variants in ceramide synthase 1 and 2 (*CERS1/2*) are associated with progressive myoclonic epilepsy, generalized tonic-clonic seizures, tremor, dysarthria, ataxia, and developmental delay (OMIM #616230) (13–15). Mutations in the GM3 synthase gene (*ST3GAL5*) lead to refractory epilepsy, psychomotor delay, blindness, and deafness (OMIM #609056) (16, 17), and GM2/GD2 synthase mutations (*B4GALNT1*) lead to GM3 accumulation and a complex form of hereditary spastic paraplegia with cognitive impairment and seizures (OMIM #609195) (18). Recently, mutations in *SGPL1* were associated with a broad spectrum of disease phenotypes including recessive steroid-resistant nephrotic syndrome (SRNS), ichthyosis, adrenal insufficiency, immunodeficiency, and brain defects (OMIM #617575) (19–21), but also with axonal peripheral neuropathy without renal or adrenal deficiencies (22).

Here, we identify *DEGS1* dysfunction as the cause of an SL disorder with leukodystrophy and hypomyelination of the peripheral nervous system.

Results

Clinical description and genetic analysis. The 22-year-old male patient was the first born of healthy consanguineous Turkish parents and showed a progressive mixed pyramidal and extrapyramidal movement disorder as well as a progressive cerebellar atrophy. At the age of 6 months a motor developmental delay was observed and progressive spasticity became obvious in the subsequent clinical course (Figure 1, A–D, and Supplemental Video; supplemental material available online with this article; https://doi.org/10.1172/JCI124159DS1). Consecutive brain MRI revealed a general hypomyelination, a thinning of the brainstem and occipital white matter, severely reduced volume of both thalami, progressive cerebellar and supra- and infratentorial atrophy, and a thin corpus callosum, most pronounced in the dorsal part (Figure 1, E–J). In the clinical course, he developed a pathological EEG with epilepsy and grand mal seizures, which were successfully treated by a combination of valproate and carbamazepine. He showed a progressive neurological dysfunction, microcephaly, dystrophy, a progressive scoliosis, neurogenic bladder, and gastroesophageal reflux. Since the age of 18 years, feeding required a percutaneous endoscopic gastrostomy. Progressive spasticity resulted in flexion contractures of the extremities, a positive Babinski sign, and increased muscle tone. At the age of 19 years, intrathecal baclofen pump therapy was initiated. Detailed clinical findings are summarized in Table 1. A muscle and sural nerve biopsy was performed at the age of 2 years. Archived electron micrographs (Figure 1, K–N) from the sural nerve biopsy showed several nerve fibers with disproportionately thin myelin sheaths, moderate myelin folding, widening of the ER of Schwann cells, and several autophagic vacuoles in the cytoplasm of Schwann cells. The muscle biopsy revealed neurogenic muscular atrophy according to the records that could be retrieved; however, no muscle specimens were available for review. Electroneurography at both arms and legs showed significantly slowed nerve conduction velocities, with only a slight reduction of the amplitudes, in line with a predominant demyelinating neuropathy. Metabolic screening for lysosomal storage disorders did not show pathological findings. Genetic workup revealed a normal male karyotype (46, XY) and array-CGH was unsuspicious (data not shown).

Using whole-exome sequencing in the index patient, his 2 unaffected siblings, and both parents revealed a suspicious homozygous missense variant in the index patient in *DEGS1* (NM_003676.3) (Figure 1, O–Q and Supplemental Table 1). Both parents and the siblings were heterozygous carriers of this *DEGS1* variant (Figure 1O). The variant changes codon 280 from alanine to valine (p.Ala280Val) (Figure 1P), affecting a highly conserved nucleotide (c.839C>T) and amino acid (Figure 1Q). The altered residue is located in the fatty acid desaturase/SL Δ4-desaturase domain. The variant was not present in public databases (dbSNP, 1000 Genomes, ESP server, ExAC, and gnomAD) and was predicted to be deleterious by several bioinformatics pathogenicity pre-

Table 1. Clinical findings in the affected individual

Parameters	Findings
DEGS1 (NM_003676.3)	c.839C>T; p.Ala280Val
Chromosomal position (hg19)	chr1:224380047C>T
Origin	Turkey (consanguineous parents)
Gender	Male
Age at onset	6 months
Age at last followup	21 yr
Clinical diagnosis	Multisystem disorder with progressive tetraspasticity, epilepsy, mental retardation, microcephaly
Clinical phenotype at last followup	Intellectual disability, nonambulatory, severe spasticity, nonverbal, friendly
Body weight	Normal at birth, dystrophy since the age of 3 yr; at last followup 43 kg (−3.7 SD); percutaneous gastrostomy since age 18 yr
Body length	Normal at birth, mild short stature since the age of 4.5 yr; at last followup 160 cm (−2.5 SD)
Head circumference	Normal in the first year then progressive microcephaly; at last followup 53 cm (−2.5 SD)
Epilepsy	Onset 5 years, grand mal epilepsy; under therapy with valproate and carbamazepine, no seizures since age 11 yr
Brain MRI	Cerebellar atrophy, mild global atrophy, thin white matter especially in the posterior brain regions
Visual evoked potentials	Pathological latency
Acoustic evoked potentials	Pathological latency
BERA	Pathological interpeak latency/auditory threshold 85 db
Electroneurography	Mild demyelinating neuropathy with decreased mNCV: medianus mNCV 30.0 m/s age 2 yr, 28.7 m/s age 12 yr; tibialis mNCV 38.0 m/s age 2 yr, 39.2 m/s age 12 yr
Nerve biopsy	Peripheral hypomyelination
Muscular biopsy	Neurogenic muscular atrophy
Scoliosis	Scoliosis surgery at age 18 yr
Neurogenic bladder disorder	Present

BERA, brainstem evoked response audiometry; mNCV, motoric nerve conduction velocity; yr, years.

diction tools (CADD phred [score 35], SIFT [score 0], Polyphen2 HDIV [score 0.99], and MutationTaster prediction [score D]).

Splicing, subcellular localization, and expression of mutant DEGS1. Besides a codon change from alanine to valine (p.Ala280Val), the software tools NNSplice and GeneSplicer predicted a possible splicing effect for the c.839C>T variant in *DEGS1*. To address an influence on splicing, we used third-generation long-read nanopore sequencing of cDNA from patient fibroblasts and did not observe aberrant transcripts compared to cDNA from control fibroblasts and reference transcripts (Figure 2A).

To investigate whether the p.Ala280Val variant (mut DEGS1) affects subcellular localization, we overexpressed EGFP-tagged wild-type (WT) and mut DEGS1 in HeLa cells. Cells were costained with markers for the ER and mitochondria (Figure 2, B–E). Both WT and mut DEGS1 colocalized with the ER marker protein disulfide isomerase (PDI) (Figure 2, B and C) and showed only little colocalization with the mitochondrial marker Tim23 (Figure 2, D and E). Notably, DEGS1 expression levels were reduced in patient fibroblasts compared with controls, as determined by Western blot (Figure 2, F and G). To further analyze the DEGS1 mutation, *DEGS1* and the homologous *DEGS2* were knocked out in HAP1 cells by CRISPR/Cas9 technology (*DEGS1*$^{-/-}$, *DEGS2*$^{-/-}$). Similarly to the expression in fibroblasts, overexpression of mut DEGS1-EGFP in HAP1 cells resulted in a lower protein amount compared with WT DEGS1-EGFP (Figure 2, H and I). FACS measurements of HAP1 WT cells transfected with WT or mut DEGS1 fused to EGFP in addition showed a lower number of GFP-positive cells (Supplemental Figure 1). Moreover, inhibiting protein translation with cycloheximide in HAP1 WT cells overexpressing either WT or mut DEGS1-EGFP indicated a reduced half-life of the mutant. In contrast, treating cells with the proteasome inhibitor MG-132 stabilized both WT and mut DEGS1 protein (Figure 2, H and J). This implies that the mutation p.Ala280Val affects overall DEGS1 protein stability.

SL analysis. We performed an untargeted lipidomics analysis from plasma of the index patient, his parents, and 6 unrelated controls. Total SL plasma levels were comparable between the individuals; however, the patient plasma revealed a striking overrepresentation of dihydrosphingolipid (dhSL) species (dhSM, dhCer, and dhHexCer) compared with parents and controls (Figure 3A). The relative proportion of dhSLs in patient plasma was approximately 40%, while it was about 10% in controls and parents. This disproportion was confirmed in patient-derived skin fibroblasts. SL de novo synthesis was measured by culturing the fibroblasts in the presence of stable isotope–labeled d4-serine, which is incorporated in de novo–formed sphingoid bases. Like in plasma, we observed a significantly increased formation of dhSL species in patient fibroblasts compared with control cells (Figure 3B). To confirm that this shift is directly caused by DEGS1 dysfunction, we used the *DEGS1* and *DEGS2*-deficient HAP1 lines. In *DEGS1*$^{-/-}$ cells, approximately 90% of the de novo–formed SLs were present in the saturated dihydro form, whereas *DEGS2*$^{-/-}$ cells showed no changes in the profile. Interestingly, the relative levels of dhSLs were lower in patient-derived fibroblasts (40%) compared with *DEGS1*$^{-/-}$ cells (90%), suggesting that the DEGS1 p.Ala280Val mutant may have some residual activity. We therefore analyzed DEGS1 activity in patient fibroblasts by measuring the conversion of stable isotope–labeled d7-sphinganine (d7SA) to d7-sphingosine (SO+7) (Figure 3C). In patient fibroblasts, a slow conversion between the 2 forms was observed, indicating that the p.Ala280Val mutant still has some activity. Compared with control fibroblasts, the rate was approximately 5-fold lower, indicating a residual activity of approximately 20%. This remaining activity was completely suppressed in the presence of the DEGS1 inhibitor fenretinide (4-HPR) (Figure 3C).

DEGS1 deficiency results in the formation of a potentially novel sphingoid base. Surprisingly, when analyzing the sphingoid base profile in hydrolyzed plasma samples we observed a second peak that was isomeric to SO. The peak was detected in the patient plasma but not in plasma of the parents or unrelated controls (Figure

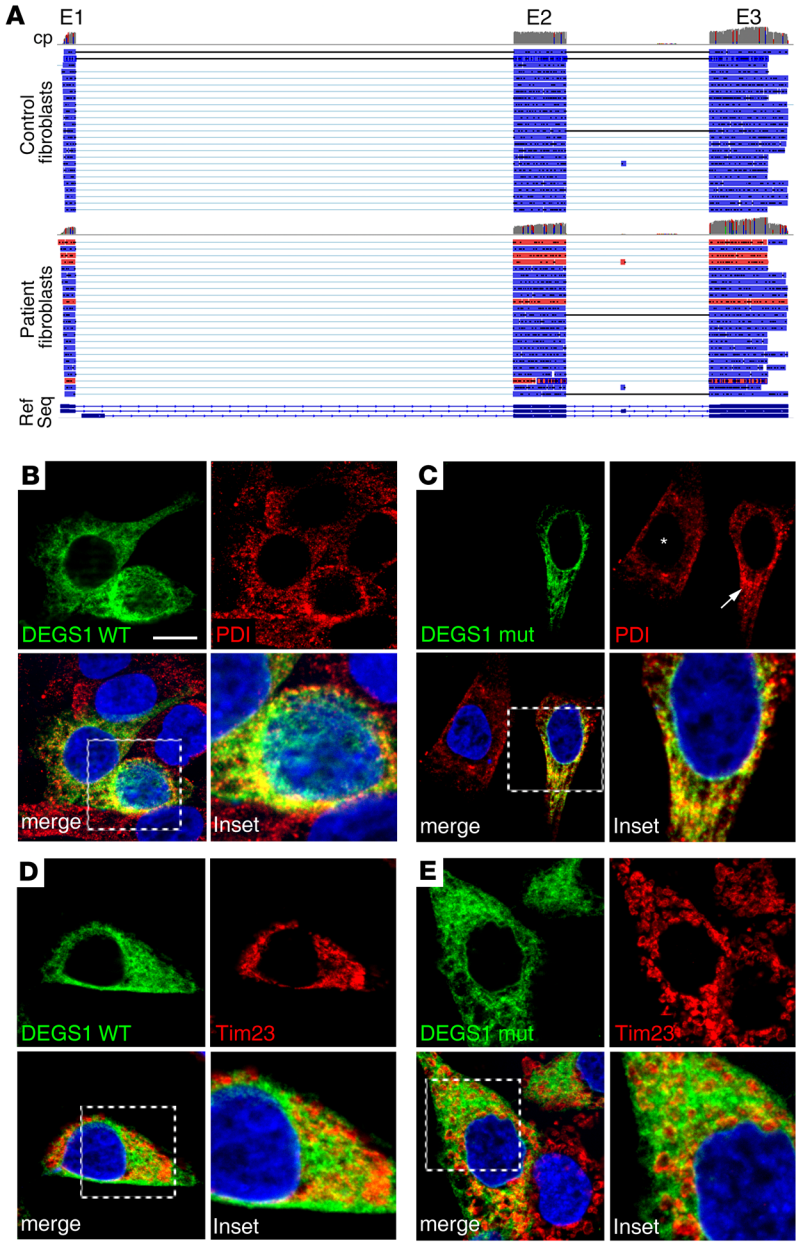

Figure 2. Characterization of mutant DEGS1 protein. The DEGS1 p.Ala280Val mutation decreases protein stability. (**A**) IGV plots of direct cDNA nanopore sequencing results. The upper part of each plot shows the coverage plot (cp, gray) and the lower part the single reads. (**B**–**E**) Cellular distribution of DEGS1 WT and the DEGS1 mutant (p.Ala280Val). EGFP-tagged (**B**) WT and (**C**) mutant DEGS1 colocalize with the endoplasmic reticulum marker protein disulfide isomerase (PDI). The reticular staining pattern of PDI in untransfected cells (asterisk in **C**) seems undisturbed in mut DEGS1–overexpressing cells (arrow in **C**). (**D** and **E**) Only minor overlap of immunofluorescence signals is observed for EGFP-tagged WT– and mut DEGS1–overexpressing cells with the mitochondrion inner membrane marker Tim23. Scale bar: 10 μm; insets show 2-fold magnification. (**F** and **G**) DEGS1 expression was analyzed by Western blot in HAP1 WT and HAP1 *DEGS1*$^{-/-}$ cells or fibroblasts from a healthy control and the index patient. (**G**) Reduced DEGS1 protein levels in patient fibroblasts, quantified from the blot in **F** (normalized to α-tubulin and the control sample). (**H**) DEGS1-EGFP expression in HAP1 WT cells transfected with pEF1α-WT DEGS1-EGFP or mut DEGS1-EGFP after treatment with cycloheximide (CHX) and MG-132 for the indicated times. (**I** and **J**) Quantification of WT and mut DEGS1-EGFP protein amounts from **H** normalized to α-tubulin and DEGS1-EGFP (**I**) or WT DEGS1-EGFP and mut DEGS1-EGFP (**J**).

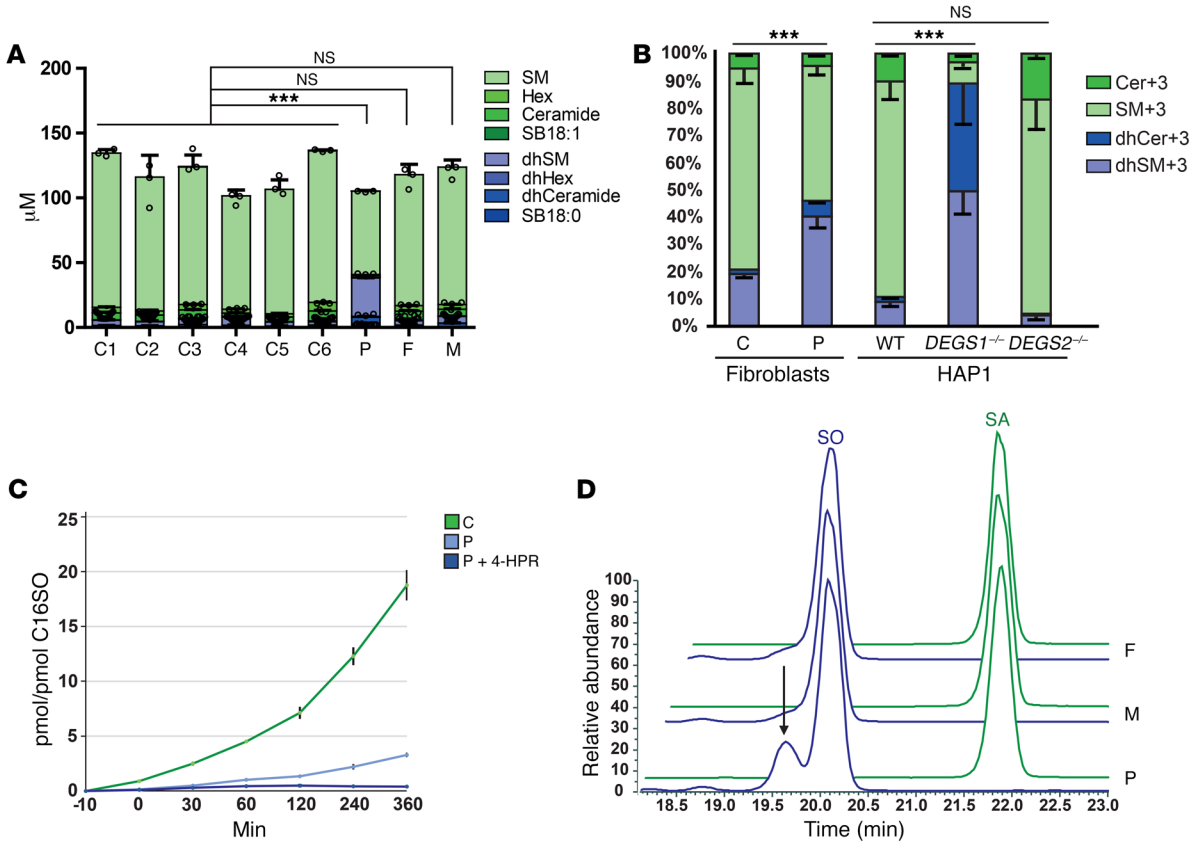

Figure 3. Lipidomics analysis of mutant DEGS1. (**A**) Lipidomics analysis showed a significant elevation of dhSL species (dhCer, dhSM, and dhHexCer) in patient plasma (P) compared with parents (F, M) or unrelated controls (C1–6). (**B**) Cultured patient-derived fibroblasts showed an increase in de novo–synthesized dhSL (dhCer+3 and dhSM+3) compared with cells from unrelated controls. Increased dhSL levels were also seen in *DEGS1*$^{-/-}$ HAP1 cells where the dhSL species reached up to 90% of the total SLs. In contrast, WT cells had less than 15% dhSL species. Slightly decreased dhSL levels were observed in *DEGS2*$^{-/-}$ cells. (**C**) Kinetics of the DEGS1 reaction in control and patient fibroblasts. Cells were supplemented with 2 µM d7SA (arrow) and the increase in total SO+7 was followed over time. Values were normalized to internal C16SO levels (ISTD). In patient-derived fibroblasts, DEGS1 activity was 5-fold lower compared with controls. This residual activity was fully inhibited in the presence of the DEGS1 inhibitor 4-HPR (2 µM). (**D**) The sphingoid-base profile after hydrolysis revealed an isomeric SO metabolite (arrow) with an approximately 30-second-shorter retention time. The metabolite could be detected in the patient plasma but not in plasma of the parents or unrelated controls. No isomeric peak was seen for SA (green). $n = 3$; data presented as the mean ±SD or –SD. ***$P < 0.001$ by 1-way ANOVA with Tukey's correction for multiple testing.

3D). The metabolite had the same mass as SO, but a 30-second-earlier retention time. To confirm that this peak is a bona fide sphingoid base, we performed an isotope labeling assay, supplementing d4-serine to HAP1 WT and *DEGS1*$^{-/-}$ cells. This resulted in the formation of canonical SO+3 in HAP1 WT cells and in the +3-labeled isomeric peak in *DEGS1*$^{-/-}$ cells (Figure 4A). The same labeling pattern was observed in control fibroblasts when DEGS1 activity was inhibited with 4-HPR (Figure 4A), confirming that this metabolite is directly associated with reduced DEGS1 activity. Furthermore, the metabolite was not formed when SPT activity was inhibited with myriocin, indicating that the formation is downstream of SPT (Supplemental Figure 2A). To gain further insight into the metabolic origin of this atypical sphingoid base, we supplemented *DEGS1*$^{-/-}$ cells with isotope-labeled d7SA or d7SO. In d7SA-supplemented cells the isomeric metabolite was formed quantitatively and isotope labeled (+7), whereas d7SO was not converted and reappeared in the cells as SO+7 with the expected retention time for the canonical SO. This indicated that the metabolite is indeed a downstream product of SA and not a direct product of SPT (Figure 4B). A structural analysis using chemical derivatization with dimethyl disulfide followed by collision-induced HCD fragmentation (23) revealed a specific fragment (*m/z* 110.10156), reflecting an isotope-labeled 4-carbon tail fragment of SO+7 (Figure 4C). An analogous nonlabeled fragment was also identified in SO-supplemented cells (Supplemental Figure 2B). These results suggest that the double-bond position of the isomeric SO metabolite is in the Δ14 position and distinct from the Δ4 position of canonical SO. This result was further confirmed by supplementing *DEGS1*$^{-/-}$ cells with d4(C_{11}-C_{12})–labeled palmitate. When incorporated into the sphingoid base, the d4(C_{11}-C_{12})–labeled palmitate is converted to SA+4 with four deuterium labels at the C_{13}-C_{14} position (Supplemental Figure 2C). Introducing a Δ4 double bond will not affect the label, whereas a Δ14 double bond results in the loss of 1 deuterium. As expected, canonical SO (Δ4) was found to be exclusively +4 labeled (Supplemental Figure 2C), whereas the isomeric pre-peak contained the +3 label, which further supports a Δ14 position of the double bond.

Supplementation of an SL-rich diet as a therapeutic intervention. Correcting the altered dhSL/SL ratio in the patient was considered

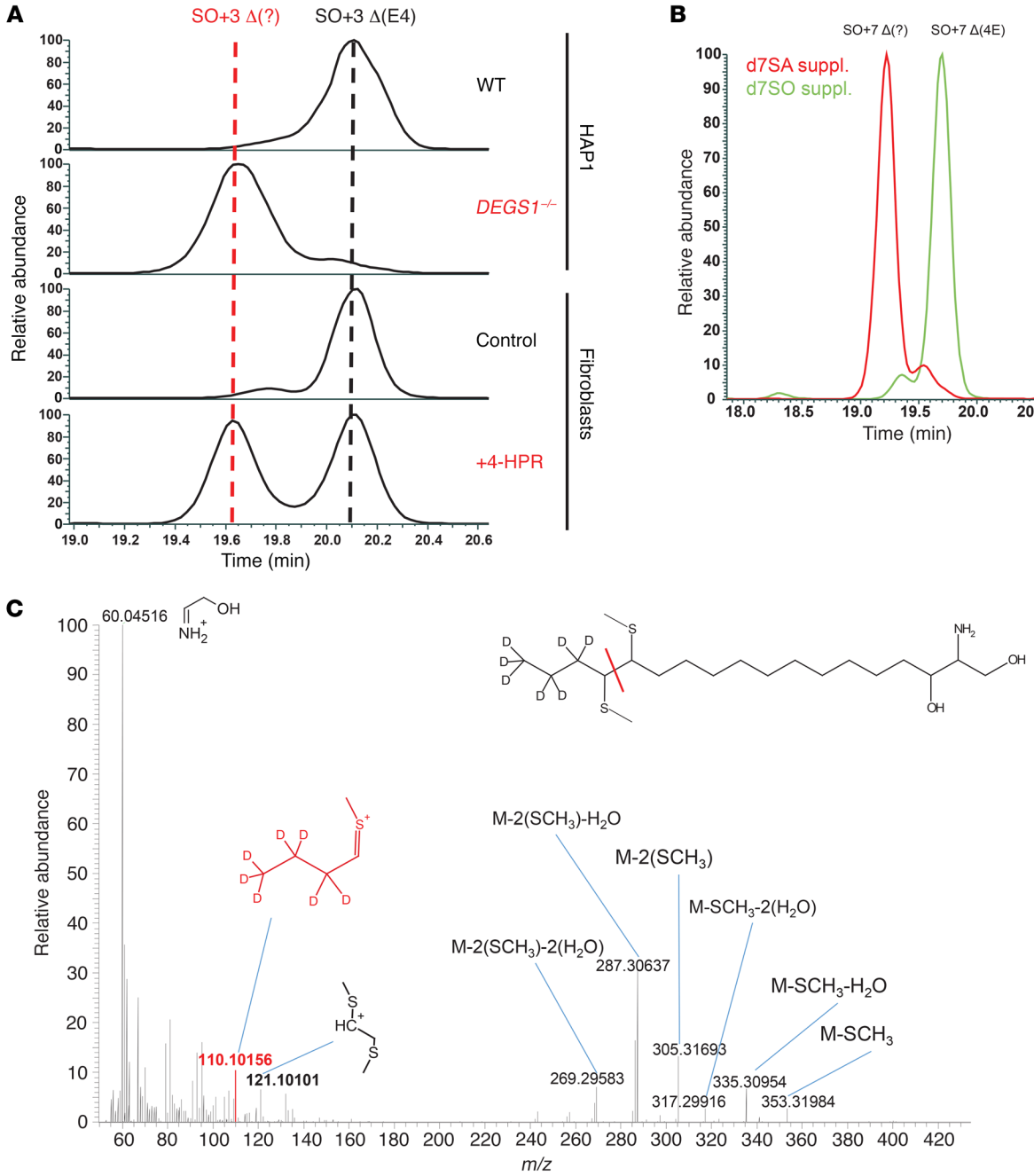

Figure 4. Characterization of a previously unidentified sphingoid base in the DEGS1 disorder. (**A**) HAP1 WT or *DEGS1*$^{-/-}$ cells were cultured in the presence of isotope-labeled d4-serine. Whereas HAP1 WT cells only formed canonical SO+3, *DEGS1*$^{-/-}$ cells exclusively formed the SO+3 isomer. Similarly, WT fibroblasts primarily formed canonical SO+3 when cultured in the presence of d4-serine, while the SO+3 isomer was formed when DEGS1 activity was inhibited with 4-HPR. (**B**) *DEGS1*$^{-/-}$ cells were supplemented with isotope-labeled d7SA (1 μM) or d7SO (1 μM) for 24 hours. The isomeric SO was formed only in d7SA-, but not in d7SO-supplemented cells. (**C**) Structural analysis of the +7-labeled isomeric SO [SOΔ(?)] after chemical derivatization with dimethyl disulfide. A specific collision fragment with *m/z* 110.10156 reflecting the isotope-labeled 4-carbon tail of SO+7 confirmed that the double bond of the isomeric SO isomer is in the Δ14 position.

as a potential therapeutic approach for the DEGS1-related disorder. SLs are abundantly present in meat, milk, and egg products (24), whereas plants and yeast usually have phytosphingolipids (phytoSLs) that bear a C4 hydroxyl group instead of the Δ4 double bond. An increased dietary SL consumption from animal products might therefore increase the levels of unsaturated SL species, thereby lowering the dhSL/SL ratio in the patient. Therefore, we tested whether the SL profile of the patient may be positively influenced by dietary intervention. The pilot study started with a 2-week washout phase providing a primarily plant-based vegetarian diet. Subsequently, the patient was fed with an animal-based diet (milk, eggs, and meat) for another 2 weeks. Plasma samples were taken before and after the washout phase and at the end of the supplementation period. The patient reported no adverse side

effects except for improved bowel movement during the vegetarian diet. However, the supplementation only had a minor effect on the plasma sphingoid-base profile (Supplemental Figure 2D). We observed a small increase in phytoSL levels after the vegetarian phase and in total SL levels at the end of the supplementation period, but no significant change in the dhSL/SL ratio.

Discussion

Here, we report on a 22-year-old male patient with a multisystem disease with hypomyelination and degeneration of both the central and the peripheral nervous systems. Leading symptoms were early-onset developmental delay, movement disorder, progressive spasticity, and epilepsy. Similar disease hallmarks may be seen in mitochondriopathies, neuronal ceroid lipofuscinosis, lysosomal storage disorders, or leukodystrophies; however, none of these diagnoses could be confirmed in the index patient. Instead, whole-exome sequencing identified a single nucleotide exchange in *DEGS1* (c.893C>T) leading to an amino acid exchange (p.Ala280Val) in a highly conserved region of the respective protein. DEGS1 is a central enzyme in the SL de novo synthesis pathway (Supplemental Figure 3) and has not yet been associated with a human monogenic disease. The enzyme catalyzes the final conversion of dhCer into ceramide by introducing a Δ4,5 *trans* double bond into the sphingoid base backbone (25). DEGS1 is a transmembrane protein residing in the ER and contains 3 conserved histidine-based motifs characteristic of membrane lipid desaturases and membrane hydrocarbon hydroxylases (5, 26, 27). Both pharmacological and genetic ablation of DEGS1 lead to an accumulation of its substrate dhCer (28). Both dhCer and ceramide can be metabolized to complex SLs, although the majority of SLs contains a SO(Δ4E), whereas SA-based dhSL species are minor. However, lipidomics analysis of the patient plasma revealed significantly elevated dhSL levels, indicating that the desaturase activity in the p.Ala280Val variant is reduced. Elevated levels of dhSL species were also seen in patient-derived fibroblasts and kinetic studies revealed a residual enzyme activity of approximately 20% for mutant compared with WT protein. Mutant DEGS1 showed a reduced expression in skin-derived fibroblasts and expression levels in transfected HAP1 cells were reproducibly lower than for the WT. Western blot quantification showed an approximately 80% reduced expression of the mutant protein in patient fibroblasts, which could explain the 20% residual activity of DEGS1 in these cells.

DEGS2, a homologous isoform of DEGS1 (29), was reported to act as a bifunctional enzyme with either C4-monooxygenase activity adding a hydroxyl group to the C4 position in forming phytoSLs, or a Δ(4)-desaturase activity similar to DEGS1. However, DEGS2 was not able to compensate for the enzymatic loss in DEGS1-deficient HAP1 cells, indicating mutually exclusive roles for both homologs.

In mice, homozygous deletion of *Degs1* (*Degs1*$^{-/-}$ mice) is lethal, although with incomplete penetrance. Surviving pups were small and revealed a complex phenotype including scaly skin and sparse hair, tremor, and metabolic abnormalities (28). *Degs1*$^{-/-}$ mice had lower ceramide levels and dramatically more dhCer in blood and tissues compared with WT littermates. Heterozygous *Degs1*$^{+/-}$ animals showed improved insulin sensitivity on high-fat diet and were resistant to dexamethasone-induced insulin resistance (28). This and subsequent observations indicated that a moderate increase in the dhCer/ceramide ratio is linked to an improved glucose metabolism and metabolic control, although the underling physiological mechanisms are not yet fully understood (30, 31). Notably, we did not observe a significant difference in the dhSL levels between the heterozygous parents and unrelated controls.

An increased dhSL/SL ratio results in higher rigidity of the plasma membrane (32), which likely affects many biological processes relying on appropriate membrane dynamics for active transport, diffusion, vesicle formation, and signaling. It is tempting to speculate that alterations in the ER structure, as observed in the EM of the sural nerve of the patient, may reflect impaired membrane properties. However, defects in DEGS1 not only influence the dhCer/ceramide ratio but also the profile of complex SLs like (dh)SM and (dh)HexCer, which are formed downstream of dhCer. SM is an abundant component of glia and myelin, and the distinct biophysical properties of dhSM might significantly affect the physiology of glial cells and the structure of the myelin sheath. Indeed, myelin has a special membrane structure with a unique molecular composition and architecture. The most striking features are high levels of plasmalogens and the enrichment of specific glycosphingolipids. Several structural aspects distinguish glycosphingolipids in myelin from glycosphingolipids found in the plasma membrane of most other cell types. In particular, the head groups are primarily based on galactose instead of glucose, a relatively high proportion of hydroxylated fatty acids, and the incorporation of very-long-chain fatty acids with chain lengths up to 26 carbons are characteristic. Even minor perturbations in this molecular composition lead to myelination defects (33), which likely explains the hypomyelination in our patient.

In addition to the increased dhSL levels, we also identified an atypical SL metabolite that seems to be specifically formed under conditions of reduced DEGS1 activity. This metabolite was isomeric to SO but eluted with a slightly shifted retention time compared with canonical SO. This metabolite was prominently present in plasma of the index patient, in *DEGS*$^{-/-}$ HAP1 cells, as well as in fibroblasts treated with the DEGS1 inhibitor 4-HPR. Isotope-labeled d4-serine confirmed that it is a bona fide SL and downstream product of SPT that can be directly formed from d7SA but not from d7SO. Further structural elucidations revealed that this isomeric SO contains a double bond at Δ14 instead of the Δ4 position. Sphingoid bases with a Δ14 double bond have been reported previously. First for sphingadienine, a polyunsaturated downstream metabolite of SO, and recently for 1-deoxySO, an aberrant sphingoid base formed by mutant SPT enzymes in the context of sensory and autonomic neuropathy type 1 (23). In both cases, the Δ14 double bond was found to be in the *cis* (Z) conformation, which likewise suggests a Δ14 double bond of the isomeric SO in *cis* (Z) conformation [SO(14Z)]. The double bond is likely formed by a not yet identified Δ14-15Z desaturase in an alternative reaction to that catalyzed by DEGS1. The toxicity and pathophysiological relevance of this atypical SO isomer is not clear, but may be a crucial part of the pathomechanism. As a *cis* (Z) conformation introduces a kink into the structure of the sphingoid base, its lateral assembly with other membrane lipids will differ from canonical SO that contains a straight (Δ4E) double bond. Both the elevation in dhSL species and the SO(14Z) isomer might be relevant for the observed hypomyelination phenotype.

In a pilot experiment we tested whether the serum dhSL/SL ratio could be influenced by a diet rich in canonical SLs. However,

we were not able to modulate the dhSL/SL ratio in the patient; this 2-week test phase may be too short or the dietary intervention to inefficient to observe a significant metabolic effect.

In summary, we identified *DEGS1* as a disease-causing gene implicated in a heritable multisystem disorder with hypomyelination and degeneration of both the central and the peripheral nervous systems. The mutation affects de novo SL synthesis, leading to an altered dhSL/SL ratio and results in the formation of an aberrant and potentially neurotoxic SO isomer.

Methods

Neuropathology. Resin embedding of the glutaraldehyde-fixed sural nerve biopsy tissue and subsequent electron microscopy was performed using standard procedures (34).

Whole-exome sequencing. Whole-exome sequencing was performed with the DNA from peripheral blood of 5 family members including the index case, 2 unaffected siblings, and both parents. Enrichment was done with an Illumina Enrichment Kit (Nextera Rapid Capture Exome v1.2) and the respective libraries were sequenced on a NextSeq500 sequencer (Illumina). Alignment and variant calling was performed with SeqMule (version 1.2) (35), FastQC (version 0.11.2), BWA-MEM (version 0.7.8-r455), SAMtools (rmdup, version 0.1.19-44428cd), SAMtools (filter, version 0.1.19-44428cd), SAMtools (index, version 0.1.19-44428cd), and GATKLite (realign, version 2.3-9-gdcdccbb). Genome version hg19 was used for the alignment. Three variant callers were applied for variant detection: GATKLite UnifiedGenotyper (variant, version 2.3-9-gdcdccbb); SAMtools (mpileup, version 0.1.19-44428cd); and FreeBayes (version 0.9.14-14-gb00b735). Variants called by at least 2 programs were considered for further analysis. The resulting variant files were combined (GATK, v3.6, CombineVariants) and processed with KGGSeq (v1.0, 14 April, 2017) (36). Variants with a minor allele frequency in public databases (i.e., ExAC, GnomAD, ESP, 1000 Genomes) above 0.75% were excluded. Average coverage in the target region was 90× to 142×, with 88%–92% above 20× coverage. Mutations were confirmed by Sanger sequencing with a BigDye Terminator 3.1 Cycle Sequencing Kit and Genetic Analyzer 3500 (ThermoFisher Scientific).

Cells and cell culture. *DEGS1*$^{-/-}$ and *DEGS2*$^{-/-}$ HAP1 cells were generated by a commercial service (Horizon Discovery). The introduction of a frame-shift mutation was confirmed by sequencing. HAP1 WT cells were provided as controls. HAP1 cells were cultured in Iscove's Modified Dulbecco's Medium (IMDM, ThermoFisher Scientific) supplemented with 10% fetal calf serum (FCS), 4 mM L-glutamine, and 1% penicillin/streptomycin at 37°C in 5% CO_2 atmosphere. Patient fibroblasts were derived from a tissue biopsy in the index patient. HeLa (ATCC, CCL-2) and BJ-5ta (ATCC, CRL-4001) cells were cultured in Dulbecco's Modified Eagle's Medium (DMEM, ThermoFisher Scientific) supplemented with 10% FCS and 1% penicillin/streptomycin at 37°C in 5% CO_2 atmosphere. Transfection of HeLa cells and HAP1 cells was done using Polyjet or GenJet in vitro transfection reagent (SignaGen) according to the manufacturer's protocol.

Immunohistochemistry. Transfected cells were fixed after 24 hours with 4% paraformaldehyde in PBS. After blocking and permeabilization with 2% bovine serum albumin, 10% normal goat serum, and 0.25% Triton X-100 in PBS for 60 minutes at room temperature, cells were incubated with primary antibodies in blocking solution for 60 minutes at room temperature, washed 3 times in PBS, and incubated with Alexa Fluor 568– or 647–labeled secondary antibodies (1:1,000; Molecular Probes). DAPI (4′,6-diamidino-2-phenylindole; 1:1,000; Invitrogen) was used for nucleic acid staining. Images were taken with a Zeiss Observer Z.1 microscope equipped with an Apotome2 and HXP 120 lamp. The following primary antibodies were used: mouse anti-PDI (Enzo, ADI-SPA-891, 1:200), mouse anti-Tim23 (BD, 611222, 1:200).

Cycloheximide chase. Transfected HAP1 cells were treated with cycloheximide (25 μg/ml) with or without 10 μM MG-132 for the indicated time period. Cells were harvested with cell scrapers in ice-cold PBS and pelleted by centrifugation at 500 *g* for 5 minutes.

Western blot. Protein isolation and Western blot were carried out as described elsewhere (37). The primary antibodies used for immunodetection were DEGS1 (Abcam, ab167169; 1:5,000), GFP (Millipore, MAB3580; 1:1,000), and α-tubulin (Abcam, ab15246; 1:2,000). As secondary antibodies, horseradish peroxidase–conjugated anti-rabbit (Santa Cruz Biotechnology, sc-2370; 1:10,000) and anti-mouse IgGs (Santa Cruz Biotechnology, sc-2005; 1:10,000) were used. Detection was done using Clarity Western ECL Substrate (Bio-Rad) and a Fuji-Film LAS 3000 system. PageRuler or PageRuler Plus Prestained Protein Ladder (ThermoFisher Scientific) was used for protein molecular weight estimation.

Cloning. Human DEGS1 (NM_003676.3) was amplified from a commercially available cDNA library using the following primers: forward, CACCATGGGGAGCCGCGTCTCGCGGGAAGACTTC; reverse, CTCCAGCACCATCTCTCCTTTTTGGTG). The amplicon for DEGS1 lacking the stop codon was subcloned into the pEGFP vector (Clontech). The mutation p.Ala280Val was introduced by targeted mutagenesis. pEF1α-DEGS1-EGFP and DEGS1-EGFP (c.893C>T) were generated by cutting pEGFP-DEGS1 with AflII and EcoRI and blunting with Klenow fragment. pEF1α-Tet3g was digested with EcoRI and HindIII and ends were filled by Klenow fragment followed by dephosphorylation with FastAP. The resulting fragments were ligated with T4 ligase. All inserts were sequence verified using Sanger sequencing.

FACS. Transfected cells were trypsinized, pelleted, and resuspended in PBS containing 250 ng/ml 7-AAD (BioLegend) for live/dead cell discrimination. Measurements were carried out on a FACSCanto II flow cytometer (Becton Dickinson). For lipidomics, cell pellets were resuspended in PBS containing 250 ng/ml 7-AAD and 20% FCS. Sorting was carried out on a FACSAria II cell sorter (Becton Dickinson) and 300,000 GFP-positive and -negative cells were collected per sample.

Lipidomics. Lipid extraction was performed as described previously (38) with some modifications. Plasma sample (20 μl) or 0.5–5 million cells were suspended in 20 μl PBS, and 1 ml of a mixture of methanol/MTBE/chloroform (MMC) 4:3:3 (v/v/v) was added. The MMC mix was fortified with 100 pmol/ml of the following internal standards: d7SA (d18:0), d7SO (d18:1), dhCer (d18:0:12:0), ceramide (d18:1/12:0), glucosylceramide (d18:1/8:0), SM (18:1/12:0), and 50 pmol/ml d7-S1P. After brief vortexing, the samples were continuously mixed in a Thermomixer (Eppendorf) at 37°C (1,400 rpm, 20 minutes). Protein precipitates were obtained after centrifugation (5 minutes, 16,000 *g*, 25°C). The single-phase supernatant was collected, dried under N_2, and stored at –20°C until analysis. Before analysis, the dried lipids were dissolved in 100 μl methanol.

Liquid chromatography was done as previously described (39) with some modifications. The lipids were separated using a C30 Accucore LC column (ThermoFisher Scientific, 150 mm × 2.1 mm × 2.6 μm) and the following mobile phases: (A) acetonitrile/water (2:8) with 10 mM ammonium acetate and 0.1% formic acid, (B) isopropanol/aceto-

nitrile (9:1) with 10 mM ammonium acetate and 0.1% formic acid, and (C) methanol at a flow rate of 0.3 ml/min.

The following gradient was applied: 0.0–1.5 minutes (isocratic 70% A, 20% B, and 10% C); 1.5–18.5 minutes (ramp 20%–100% B); 18.5–25.5 minutes (isocratic 100% B); 25.5–30.5 minutes (isocratic 70% A, 20% B, and 10% C).

The liquid chromatography was coupled to a Q-Exactive hybrid quadrupole-orbitrap mass spectrometer (ThermoFisher Scientific); samples were analyzed in positive mode using a heated electrospray ionization (HESI) interface. The following parameters were used: spray voltage 3.5 kV, vaporizer temperature 300°C, sheath gas pressure 20 AU, aux gas 8 AU, and capillary temperature 320°C. The detector was set to an MS^2 method using data-dependent acquisition with top10 approach with stepped collision energy between 25 and 30. A resolution of 140,000 was used for the full spectrum and a 17,500 for MS^2. A dynamic exclusion filter was applied that excludes fragmentation of the same ions for 20 seconds. Identification criteria were (a) resolution with an accuracy of 5 ppm from the predicted mass at a resolving power of 140,000 at 200 , (b) isotopic pattern fitting to expected isotopic distribution, (c) matching retention time on synthetic standards if available, and (d) the specific fragmentation patterns. Quantification was done using single-point calibration. Pooled samples at 4 concentrations were used as quality controls.

Metabolic labeling and sphingoid-base profiling. Cells (250,000) were seeded in 2 ml fresh medium in 6-well plates (BD Falcon) and cultured for 2 days, reaching approximately 70%–80% confluence. The medium was exchanged for L-serine– and L-alanine–free DMEM (Genaxxon Bioscience), containing 10% FBS (ThermoFisher Scientific; FSA15-043) and 1% penicillin and streptomycin (100 units/ml and 0.1 mg/ml, respectively; MilliporeSigma). Two hours after medium exchange, isotope-labeled d3-^{15}N-L-serine (1 mM) and (2,3,3,3)-d4-L-alanine (2 mM) was added (Cambridge Isotope Laboratories). In certain cases, myriocin (Focus Biomolecules) or d7SA/d7SO (Avanti Polar Lipids) was also added to the cells. Palmitate labeling was performed in DMEM (MilliporeSigma) with 10% FBS and 1% penicillin and streptomycin supplemented with 25 μM d4-palmitic acid (Cambridge Isotope Laboratories). After 24 hours, cells were harvested in 1 ml cold PBS, counted (Beckman Coulter Z2), pelleted at 600 *g* at 4°C, and stored at −20°C until further processing. During the SPT reaction, 1 deuterium from serine is exchanged with a hydrogen, which results in newly formed sphingoid bases with a d3 isotope label. In some cases, the quantification of isotope-labeled sphingoid bases was simplified by hydrolyzing the extracted lipids prior to MS analysis (40). During hydrolysis, the conjugated *N*-acyl chains and attached head groups are removed and the SL backbones released as free sphingoid bases. dhSL species are converted to free SA and unsaturated species to free SO.

Dimethyl disulfide adduct analysis by LC-MS. Dimethyl disulfide (DMDS, 100 μl) and 20 μl of I_2 (in diethyl ether, 60 mg/ml) were added to whole-cell extracts or 15 nmol SPH m18:1(4E)(3OH) standard. Samples were agitated for 16 hours in an Eppendorf Thermo shaker at 1,400 rpm and 47°C. The reaction was quenched with 100 μl of 5% aqueous $Na_2S_2O_3$, extracted with 200 μl of hexane, and dried under N_2. Samples were dissolved in 50 μl methanol/water (1:1) for further analysis according to the method of Dunkelblum, Tan, and Silk (9), with some modifications. The DMDS adducts were separated using a C30 Accucore LC column (ThermoFisher Scientific, 150 mm × 2.1 mm × 2.6 μm) and the following mobile phases: (A) methanol/water (1:1) with 10 mM ammonium formate and 0.1% formic acid, and (B) methanol at a flow rate of 0.3 ml/min using a TLX Transcend pump (ThermoFisher Scientific). The following gradient was applied: (a) 0.0–1.0 minute (isocratic 10% B), (b) 1.0–26.0 minutes (ramp 10%–100% B), (c) 26.0–32.0 minutes (isocratic 100% B), (d) 32.0–33.0 minutes (ramp 100%–10% B), and (e) 33.0–35.0 (isocratic 10% B).

The liquid chromatography was coupled to a Q-Exactive hybrid quadrupole-orbitrap mass spectrometer; samples were analyzed in positive mode using a HESI interface. The following parameters were used: spray voltage 3.5 kV, vaporizer temperature 100°C, sheath gas pressure 40 AU, aux gas 10 AU, and capillary temperature 300°C. The mass spectrometer was operated in 2 alternating scan modes: (a) full scan mode at 140,000 resolution, 3×10^6 AGC target and scan range 150–900 *m/z*; and (b) parallel reaction monitoring mode (PRM) at 70,000 resolution, 2×10^5 AGC target, 200 ms maximum injection time, and 1.5 *m/z* isolation window. The normalized collision energy was set to 35, 50, and 70. The inclusion list for the PRM included both the nonlabeled SO DMDS adduct (*m/z* 394.28080) and the d7-labeled SO DMDS adduct (*m/z* 401.32473).

Statistics. Results are presented as the mean ± SD or mean – SD from at least 3 independent experiments using GraphPad Prism 8. Statistical analysis was conducted using a 2-tailed *t* test or 2-way ANOVA with Tukey's correction for multiple comparisons. A *P* value of less than 0.05 was considered statistically significant.

Study approval. Written informed consent was obtained from the study participants after approval from the Institutional Review Boards at the participating institutions (Uniklinik RWTH Aachen: EK302-16). Consent was obtained according to the Declaration of Helsinki and consent was given for the publication of patient photographs and video.

Author contributions

IK, GCK, and TH designed the study. GCK, CK, MM, and ME assessed the phenotype of the patient. M. Bergmann, JMS, and JW performed the neuropathological analysis. Exome sequencing and evaluation was done by M. Begemann, FK, and IK. Lipidomics studies were performed and evaluated by GK, AO, SS, RS, and TH. Cell biological experiments were done by FK, NH, and BH.

Acknowledgments

We are grateful to the family participating in the study. We thank Sebastian Gießelmann for excellent technical support. We thank Peter Steuernagel (Klinikum Oldenburg) for initial fibroblast cultures. This work was supported by grants from the German Charcot-Marie-Tooth Disease Network (CMT-Net; 01GM1511D) to JW; funding of the 7th Framework Program of the European Commission (RESOLVE, project number 305707); the Swiss National Foundation (SNF, project 31003A_153390/1); the Hurka Foundation; the Novartis Foundation; and the Rare Disease Initiative Zurich (radiz, Clinical Research Priority Program for Rare Diseases, University of Zurich) to TH.

Address correspondence to: Ingo Kurth, Institute of Human Genetics, Uniklinik RWTH Aachen, Pauwelsstr. 30, 52074 Aachen, Germany. Phone: 49.241.8080178; Email: ikurth@ukaachen.de. Or to: Thorsten Hornemann, Institute for Clinical Chemistry University Hospital Zurich, Rämistrasse 100, 8091 Zürich, Switzerland. Phone: 41.44.255.47.19; Email: thorsten.hornemann@usz.ch.

1. Hannun YA, Obeid LM. Sphingolipids and their metabolism in physiology and disease. *Nat Rev Mol Cell Biol*. 2018;19(3):175–191.
2. Hannun YA, Obeid LM. Principles of bioactive lipid signalling: lessons from sphingolipids. *Nat Rev Mol Cell Biol*. 2008;9(2):139–150.
3. Bikman BT, Summers SA. Ceramides as modulators of cellular and whole-body metabolism. *J Clin Invest*. 2011;121(11):4222–4230.
4. Levy M, Futerman AH. Mammalian ceramide synthases. *IUBMB Life*. 2010;62(5):347–356.
5. Ternes P, Franke S, Zähringer U, Sperling P, Heinz E. Identification and characterization of a sphingolipid delta 4-desaturase family. *J Biol Chem*. 2002;277(28):25512–25518.
6. Ogretmen B. Sphingolipid metabolism in cancer signalling and therapy. *Nat Rev Cancer*. 2018;18(1):33–50.
7. Merrill AH, et al. Sphingolipids--the enigmatic lipid class: biochemistry, physiology, and pathophysiology. *Toxicol Appl Pharmacol*. 1997;142(1):208–225.
8. Hanada K, et al. Molecular machinery for non-vesicular trafficking of ceramide. *Nature*. 2003;426(6968):803–809.
9. Bienias K, Fiedorowicz A, Sadowska A, Prokopiuk S, Car H. Regulation of sphingomyelin metabolism. *Pharmacol Rep*. 2016;68(3):570–581.
10. Adada M, Luberto C, Canals D. Inhibitors of the sphingomyelin cycle: Sphingomyelin synthases and sphingomyelinases. *Chem Phys Lipids*. 2016;197:45–59.
11. Sabourdy F, et al. Monogenic neurological disorders of sphingolipid metabolism. *Biochim Biophys Acta*. 2015;1851(8):1040–1051.
12. Astudillo L, et al. Human genetic disorders of sphingolipid biosynthesis. *J Inherit Metab Dis*. 2015;38(1):65–76.
13. Mosbech MB, et al. Reduced ceramide synthase 2 activity causes progressive myoclonic epilepsy. *Ann Clin Transl Neurol*. 2014;1(2):88–98.
14. Vanni N, et al. Impairment of ceramide synthesis causes a novel progressive myoclonus epilepsy. *Ann Neurol*. 2014;76(2):206–212.
15. Ferlazzo E, et al. Autosomal recessive progressive myoclonus epilepsy due to impaired ceramide synthesis. *Epileptic Disord*. 2016;18(S2):120–127.
16. Fragaki K, et al. Refractory epilepsy and mitochondrial dysfunction due to GM3 synthase deficiency. *Eur J Hum Genet*. 2013;21(5):528–534.
17. Simpson MA, et al. Infantile-onset symptomatic epilepsy syndrome caused by a homozygous loss-of-function mutation of GM3 synthase. *Nat Genet*. 2004;36(11):1225–1229.
18. Boukhris A, et al. Alteration of ganglioside biosynthesis responsible for complex hereditary spastic paraplegia. *Am J Hum Genet*. 2013;93(1):118–123.
19. Janecke AR, et al. Deficiency of the sphingosine-1-phosphate lyase SGPL1 is associated with congenital nephrotic syndrome and congenital adrenal calcifications. *Hum Mutat*. 2017;38(4):365–372.
20. Lovric S, et al. Mutations in sphingosine-1-phosphate lyase cause nephrosis with ichthyosis and adrenal insufficiency. *J Clin Invest*. 2017;127(3):912–928.
21. Prasad R, et al. Sphingosine-1-phosphate lyase mutations cause primary adrenal insufficiency and steroid-resistant nephrotic syndrome. *J Clin Invest*. 2017;127(3):942–953.
22. Atkinson D, et al. Sphingosine 1-phosphate lyase deficiency causes Charcot-Marie-Tooth neuropathy. *Neurology*. 2017;88(6):533–542.
23. Steiner R, et al. Elucidating the chemical structure of native 1-deoxysphingosine. *J Lipid Res*. 2016;57(7):1194–1203.
24. Vesper H, Schmelz EM, Nikolova-Karakashian MN, Dillehay DL, Lynch DV, Merrill AH. Sphingolipids in food and the emerging importance of sphingolipids to nutrition. *J Nutr*. 1999;129(7):1239–1250.
25. Causeret C, Geeraert L, Van der Hoeven G, Mannaerts GP, Van Veldhoven PP. Further characterization of rat dihydroceramide desaturase: tissue distribution, subcellular localization, and substrate specificity. *Lipids*. 2000;35(10):1117–1125.
26. Cadena DL, Kurten RC, Gill GN. The product of the MLD gene is a member of the membrane fatty acid desaturase family: overexpression of MLD inhibits EGF receptor biosynthesis. *Biochemistry*. 1997;36(23):6960–6967.
27. Sperling P, Zähringer U, Heinz E. A sphingolipid desaturase from higher plants. Identification of a new cytochrome b5 fusion protein. *J Biol Chem*. 1998;273(44):28590–28596.
28. Holland WL, et al. Inhibition of ceramide synthesis ameliorates glucocorticoid-, saturated-fat-, and obesity-induced insulin resistance. *Cell Metab*. 2007;5(3):167–179.
29. Mizutani Y, Kihara A, Igarashi Y. Identification of the human sphingolipid C4-hydroxylase, hDES2, and its up-regulation during keratinocyte differentiation. *FEBS Lett*. 2004;563(1–3):93–97.
30. Holland WL, Summers SA. Strong heart, low ceramides. *Diabetes*. 2018;67(8):1457–1460.
31. Summers SA. Could ceramides become the new cholesterol? *Cell Metab*. 2018;27(2):276–280.
32. Vieira CR, et al. Dihydrosphingomyelin impairs HIV-1 infection by rigidifying liquid-ordered membrane domains. *Chem Biol*. 2010;17(7):766–775.
33. Aggarwal S, Yurlova L, Simons M. Central nervous system myelin: structure, synthesis and assembly. *Trends Cell Biol*. 2011;21(10):585–593.
34. Nolte KW, Hans VJ, Schattenfroh C, Weis J, Schröder JM. Perineurial cells filled with collagen in 'atypical' Cogan's syndrome. *Acta Neuropathol*. 2008;115(5):589–596.
35. Guo Y, Ding X, Shen Y, Lyon GJ, Wang K. SeqMule: automated pipeline for analysis of human exome/genome sequencing data. *Sci Rep*. 2015;5:14283.
36. Li MX, et al. Predicting mendelian disease-causing non-synonymous single nucleotide variants in exome sequencing studies. *PLoS Genet*. 2013;9(1):e1003143.
37. Esmaeili M, et al. The tumor suppressor ING1b is a novel corepressor for the androgen receptor and induces cellular senescence in prostate cancer cells. *J Mol Cell Biol*. 2016;8(3):207–220.
38. Pellegrino RM, Di Veroli A, Valeri A, Goracci L, Cruciani G. LC/MS lipid profiling from human serum: a new method for global lipid extraction. *Anal Bioanal Chem*. 2014;406(30):7937–7948.
39. Narváez-Rivas M, Zhang Q. Comprehensive untargeted lipidomic analysis using core-shell C30 particle column and high field orbitrap mass spectrometer. *J Chromatogr A*. 2016;1440:123–134.
40. Alecu I, et al. Cytotoxic 1-deoxysphingolipids are metabolized by a cytochrome P450-dependent pathway. *J Lipid Res*. 2017;58(1):60–71.